A combined experimental and computational study of the flow characteristics in a Type B aortic dissection: Effect of primary and secondary tear size

Ivan Zadrazil[a], Crispin Corzo[a], Victor Voulgaropoulos[a], Christos N. Markides[a,b,*], Xiao Yun Xu[a]

[a] *Department of Chemical Engineering, Imperial College London, South Kensington Campus, London SW7 2AZ, United Kingdom*
[b] *Kutateladze Institute of Thermophysics, Novosibirsk, Russian Federation*

N.B.: This is the ACCEPTED version of this article.
The final, published version of the article, can be found at:
https://doi.org/10.1016/j.cherd.2020.05.025

Abstract

Aortic dissection is related to the separation of the tunica intima from the aortic wall, which can cause blood to flow through the newly formed lumen, thereby further damaging the torn vessel. This type of pathology is the most common catastrophic event that affects the aorta and is associated with complications such as malperfusion. In this work, an idealised, simplified geometric model of Type B aortic dissection is investigated experimentally using particle image velocimetry (PIV) and numerically using computational fluid dynamic (CFD) simulations. The flow characteristics through the true and false lumina are investigated parametrically over a range of tear sizes. Specifically, four different tear sizes and size ratios are considered, each representing a different dissection case or stage, and the experimental and numerical results of the flow-rate profiles through the two lumina in each case, along with the phase-averaged velocity vector maps at mid-acceleration, mid-deceleration, relaminarisation and peak systole, and their corresponding velocity profiles are compared. The experimental and numerical results are in good qualitative as well as quantitative agreement. The flow characteristics found here provide insight into the importance of the re-entry tear. We observe that an increase in the re-entry tear size increases considerably the flow rate in the false lumen, decreases significantly the wall shear stress (WSS) and decreases the pressure difference between the false and the true lumen. On the contrary, an increase in the entry tear, increases the flow rate through the false lumen, increases slightly the WSS and increases the pressure difference between the false and the true lumen. These are crucial findings that can help interpret medical diagnosis and accelerate prevention and treatment, especially in high-risk patients.

Keywords: aortic dissection, biofluid mechanics, computational fluid dynamics, particle image velocimetry, pulsating flows, wall shear stress

1. Introduction

Aortic dissection (AD) is the most common catastrophic event that affects the aorta and exhibits mortality rates that can be as high as 76% for Type B AD (Hagan et al., 2000). The onset of classic AD occurs with a tear in the wall of the aorta. The entering blood of pulsatile pressure further opens the tear and splits the wall layers. The aorta develops into a separate true lumen (TL) and a false lumen (FL), divided by a flap or septum (Tran and Khoynezhad, 2009). The tear, which allows blood flows inside the false lumen, is known as the entry tear. Additional tears, known as secondary tears, distal or re-entry tears, may also appear. According to the Stanford system, if the dissection involves the ascending aorta, regardless of the site of origin is known as type A, otherwise is known as Type B. Here the Type B AD will be discussed.

The incidence of AD is estimated at 5 to 30 cases per million inhabitants per year in the United States (Khan and Nair, 2002). Among the causes of the tear are untreated hypertension, advanced age, and disease of the aortic wall (Prêtre and Von Segesser, 1997). These risk factors initiate thickening and fibrosis of the inner layer of the wall and therefore, wall stiffening and weakening, leading to AD (Ramanath et al., 2009). Consequently, the geometry of the aorta and in turn its flow characteristics are affected over time. For example, some patients show changes such as expansion of the descending aorta, the true lumen and the false lumen (Blount and Hagspiel, 2009); increase in size, number, and position of the tears (Sueyoshi et al., 2009); and changes in false lumen patency (Chang et al., 2008).

*Corresponding author
Email address: c.markides@imperial.ac.uk (Christos N. Markides)

There is a great amount of evidence suggesting that haemodynamic factors contribute to the progression of the disease (Paras and Kanaris, 2019). High wall shear stresses (WSS) found at the edges of the tear are believed to lead to the expansion of the entry tear, causing additional injury to the cells and the formation of additional tears (Karmonik et al., 2012; Cheng et al., 2013). It has also been found that an increase of the true and false lumina diameter may be caused by high pressure, which deteriorates the wall cells and its properties and can lead to rupture of the wall. For this reason, an assessment of the haemodynamics is needed to understand its role in the progression of the disease.

There have been several researchers investigating AD both experimentally and numerically. Previous experimental efforts showed that in patients with only one entry tear, the false lumen blood outflow was impaired, causing the false lumen to remain pressurised, as was found by Tolenaar et al. (2013) by analysing computed tomography angiograms (CTA) from 60 patients with uncomplicated Type B AD. Furthermore, Clough et al. (2012) reported the presence of helical flows at different locations in the false lumen by examining images acquired with phase-contrast magnetic resonance imaging (PC-MRI) and related these helical flows to the aortic expansion rate. More recently, a few research groups are employing laser diagnostic methods to explore the haemodynamics in higher spatial and temporal resolution, using primarily particle image velocimetry (PIV) (Yip et al., 2004; Salameh et al., 2017, 2019; Moravia et al., 2019) and stereo-particle image velocimetry (s-PIV) (Fernandes et al., 2019).

Computational fluid dynamics (CFD) have been largely used over the years to simulate the flow during AD, and the methods, benefits and challenges associated with the adoption and translation of CFD modelling within cardiovascular medicine has been recently reviewed multiple times (Sun and Xu, 2014; Morris et al., 2016; Sun and Chaichana, 2016). While the need for more research in this area is urged by these authors, the primary conclusion reached is that WSS indeed plays a major role in the initiation, progression and destabilisation of atherosclerotic cardiovascular disease. It has also been found that the management and prognosis of AD is often challenging, and the use of personalised computational models is being explored as a tool to improve clinical outcome (Alimohammadi et al., 2014, 2015; Bonfanti et al., 2017).

Cheng et al. (2013) simulated four patient-specific dissected aortas and found that the turbulent and disturbed flow was induced by irregular geometries, such as narrow or dilated sections that also caused a variation of the flow patterns and the WSS. Similarly, Tse et al. (2012) investigated haemodynamics of six patient-specific aortas numerically and found that the presence of vortices, helix and skewness was common in complicated geometries. To determine how the anatomical and haemodynamic factors are associated with subsequent anatomical changes, CFD is used to explore the fluid-structure interactions (Sun et al., 2006; Tan et al., 2009; Torii et al., 2009), while recently, a strong case is being made that combining commonly available clinical data with computational modelling can be a powerful tool to enhance clinical understanding of AD (Cheng et al., 2015; Bonfanti et al., 2019). Towards that goal, assessing the accuracy of CFD model is crucial and combined experimental and numerical studies can accelerate such efforts as evidenced by recent work (Kousera et al., 2013; Cheng et al., 2014; Ong et al., 2019).

The overall aim of the present combined experimental and numerical investigation is to provide a detailed analysis of the influence of different tear sizes on the haemodynamics of descending ADs, with the following specific objectives:

- Design, manufacture and generate a range of physical and computational physiological AD models with different sizes of entry and re-entry tears.
- By using an appropriate pulsatile pump, perform PIV in order to characterise the flow under a range of physiological conditions in each of these models and obtain corresponding spatiotemporally resolved velocity information.
- Validate the CFD simulations against the experimentally generated data, by directly using the same (heart) flow rate data, and compare velocity profiles.
- Extract crucial information from the validated simulations, which is not immediately available from experiments, e.g., WSS and pressure difference.
- Utilise this combined information to explore the inherent link between the haemodynamics and the progression of the medical condition.

The results obtained from the parametric study utilising a combination of advanced experimental and computational tools can provide a holistic picture of the flow characteristics under different geometries and at different cardiac time-instances of the phenomenon. The ultimate goal is to illustrate the flow mechanisms that take place in a patient with AD and translate these findings to gain fundamental understanding of AD and pave the way towards more effective prevention and treatment methods.

2. Methods

This section provides a description of the AD model employed for the experimental measurements, the velocity field measurement procedure, image post-processing and data analysis as well as the CFD modelling methodology. Specifically, Section 2.1 contains the design details of the AD model, together with the experimental apparatus and the optical-based technique used to measure the velocity fields. The experimental data processing is summarised in Section 2.2, and finally, Section 2.3 contains details of the numerical method employed.

2.1. Experimental methods

2.1.1. Dissected aorta model

A model of the aorta with exchangeable partitions was used (see Figs. 1(a) and (b)). The model, made of perfluoroalkoxy (PFA), contained segments that represented the ascending thoracic aorta, the aortic arch and the descending thoracic aorta. The internal diameter (ID) was 16 mm and was kept constant for all parts of the aorta model. The aortic arch was 45 mm wide with a radius of curvature of 22.5 mm, and a length of the descending thoracic aorta of 136 mm. This geometrical size was intended to be a 1:2 scale model of an idealised (dissected) aorta.

Four different partitions, made of polymethyl methacrylate (PMMA), were used to represent the septum. All partitions had the same overall dimensions: $16 \times 136 \times 1$ mm. The partitions featured a range of openings, representing the two tears (entry with diameter d_1 and re-entry with diameter d_2). The tears were formed by drilling circular holes, which split the aorta model into true and false lumina. The centre of the entry tear was located 37 mm from the leading edge of the dissection insert and the centre of the re-entry tear was positioned 84 mm from the entry tear (see Fig. 1).

The following d_2:d_1 opening combinations are investigated in this work: 1.6:6.4; 3.2:3.2; 3.2:6.4; and 3.2:9.6 (all in cm), with corresponding abbreviations for these geometries used in this paper of: 16-64; 32-32; 32-64 and 32-96, respectively. The studied flow cases are noted in Table 1. Each partition (dissection insert) extended from the end of the aortic arch to the end of the descending aorta, and was positioned in the middle of the model of the descending thoracic aorta, separating it and creating a true and false lumen. The outlet from the false lumen was closed by using a PFA plug.

A schematic of the experimental arrangement used for the flow field measurements at the simplified model of the dissected aorta is shown in Fig. 1(c). The system comprised a mixing vessel, a pulsatile blood pump (HABP010 Pulsatile blood pump for rabbits, Instech Laboratories) and a simplified model of AD that was located in an anti-distortion borosilicate box, while the tubing, connecting the several parts together, was sealed with jubilee clips. Deionised (DI) water, with a density of $\rho = 997$ kg m^{-3} and a viscosity of $\mu = 8.9 \times 10^{-4}$ Pa s, seeded uniformly with inert particles at a concentration of 30 mg L^{-1} was used as the experimental fluid. A stirrer was used to prevent the seeding particles from settling to the bottom of the mixing vessel and to keep them homogeneously dispersed in the DI water. The volume of the liquid displaced by the pulsatile pump was 0.1 L per pulse at a pulse frequency of 70 strokes per minute.

2.1.2. Flow similarity and design of the experiments

The specific liquid, the pulsatile pump conditions (i.e., the displacement volume and the pulse frequency) and the diameter of the AD model used in this work were set in order to match dimensionless conditions between physiological and experimental flows, and hence achieve dynamic similarity between the model-system studied herein and the real physiological flow. We ensured this agreement by the design of experiment, i.e., by using different pulsation frequency and geometry dimensions compared to those encountered in the real system, so as to accommodate for the differences in the physical properties of the fluids (blood *vs* water).

Two dimensionless parameters are considered in this work, namely the Reynolds number (Re) and the Womersley number (Wo). The former characterises the ratio of inertial to viscous forces and is a measure of a turbulent character of a given flow, while the latter is a ratio of transient inertial to viscous forces and characterises dynamic similarity in pulsatile flows.

Dynamic similarity between the experimental and the physiological flows requires that the two Reynolds numbers are equal, i.e.:

$$Re_{\text{exp}} = Re_{\text{phys}} \implies \frac{U_{\text{exp}} D_{\text{exp}}}{U_{\text{phys}} D_{\text{phys}}} = \frac{\nu_{\text{exp}}}{\nu_{\text{phys}}}, \tag{1}$$

While for flow similarity with respect to the Womersley number:

$$Wo_{\text{exp}} = Wo_{\text{phys}} \implies \left(\frac{D_{\text{exp}}}{D_{\text{phys}}}\right)^2 \frac{f_{\text{exp}}}{f_{\text{phys}}} = \frac{\nu_{\text{exp}}}{\nu_{\text{phys}}}, \tag{2}$$

where U is the velocity, D the tube inner diameter, ν the kinematic viscosity, ω the angular frequency and f the frequency. The subscripts 'exp' and 'phys' refer to the experimental and physiological related quantities, respectively. From Eq. 1 and Eq. 2:

$$\frac{D_{\text{exp}} f_{\text{exp}}}{D_{\text{phys}} f_{\text{phys}}} = \frac{U_{\text{exp}}}{U_{\text{phys}}} \tag{3}$$

The flow rate Q in the experiments was set by the pulsatile pump and can be calculated by $Q_{\text{exp}} = AU_{\text{exp}} = \pi/4 D^2_{\text{exp}} U_{\text{exp}}$. Similarly, the flow rate in the physiological case can be expressed as $Q_{\text{phys}} = AU_{\text{phys}} = \pi/4 D^2_{\text{phys}} U_{\text{phys}}$, where A corresponds to the cross-sectional flow area. The ratio of the experimental and physiological flow-rates is then given by:

$$\frac{Q_{\text{exp}}}{Q_{\text{phys}}} = \left(\frac{D_{\text{exp}}}{D_{\text{phys}}}\right)^2 \frac{U_{\text{exp}}}{U_{\text{phys}}}. \tag{4}$$

Combining Eqs. 3 and 4 yields:

$$\left(\frac{D_{\text{exp}}}{D_{\text{phys}}}\right)^3 \frac{f_{\text{exp}}}{f_{\text{phys}}} = \frac{Q_{\text{exp}}}{Q_{\text{phys}}}. \tag{5}$$

The volumetric flow-rate and the frequency of the pulsatile pump were set during the experiments to satisfy the

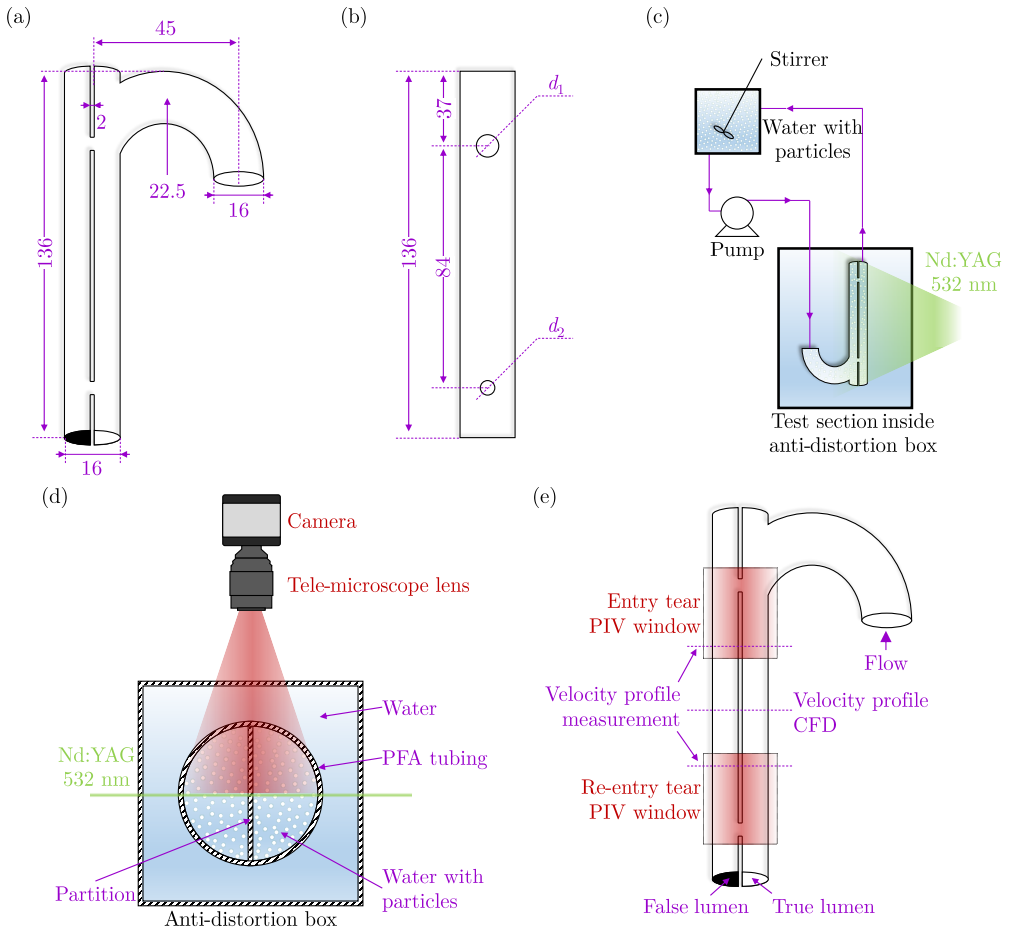

Figure 1: Arrangement of the test section of interest: (a) dissected aorta model with prescribed dimensions; (b) insert plates (flap) with prescribed dimensions; (c) schematic illustration of the apparatus; (d) PIV measurement arrangement (top view); and (e) simplified AD physical model (side view) highlighting the PIV measurement windows and the locations where velocity profiles have been extracted by PIV and predicted by CFD.

Table 1: Studied flow case properties and corresponding data.

Tear Case	Entry Tear Size, d_1 (mm)	Re-Entry Tear Size, d_2 (mm)	Re-entry to Entry Tear Ratio	Maximum TAWSS (Pa)
16-64	6.4	1.6	1:4	16
32-32	3.2	3.2	1:1	8
32-64	6.4	3.2	1:2	11
32-96	9.6	3.2	1:3	11.5

following requirements:

$$Q_{\text{exp}} = k f_{\text{exp}}; \quad k \leq V_0; \quad f_{\text{exp}} \leq f_{\text{max}}, \tag{6}$$

where V_0 is the maximum volumetric flow-rate of the pump divided by the maximum frequency $V_0 = Q_{\text{max}}/f_{\text{max}}$ and k is the proportionality factor. The characteristic values of Q_{max} and f_{max} of the pulsatile blood pump used are 2 L min^{-1} and 200 strokes per minute, respectively, hence $V_0 = 0.01$ L. If we substitute Eq. 6 into Eq. 5, we get:

$$\left(\frac{D_{\text{exp}}}{D_{\text{phys}}}\right)^3 \frac{1}{f_{\text{phys}}} = \frac{k}{Q_{\text{phys}}}. \tag{7}$$

Finally, replacing the ratio of U with the ratio of Q from Eq. 4 into Eq. 1 and using Eq. 6, we can write:

$$\frac{\nu_{\text{exp}}}{\nu_{\text{phys}}} = \frac{k f_{\text{exp}}}{Q_{\text{phys}}} \frac{D_{\text{exp}}}{D_{\text{phys}}}; \quad k \leq V_0. \tag{8}$$

Typical values of Q_{phys} and f_{phys} that can be found in the literature [e.g., Rudenick et al. (2013)] are 4-6 L min^{-1} and 60-80 strokes per minute, respectively, with mean values of $Q_{\text{phys}} = 5$ L min^{-1} and $f_{\text{phys}} = 70$ strokes per minute. Eq. 7 then becomes:

$$\frac{D_{\text{exp}}}{D_{\text{phys}}} = 2.4 k^{1/3}; \quad k \leq V_0, \tag{9}$$

and Eq. 8 becomes:

$$\frac{\nu_{\text{exp}}}{\nu_{\text{phys}}} = \frac{k^{2/3} f_{\text{exp}}}{12}, \tag{10}$$

for $k \leq V_0$ and $f_{\text{exp}} \leq f_{\text{max}}$.

In order to fulfil the similarity requirements between the experimental and physiological flows (based on Eqs. 9 and 10), the pulsatile pump and liquid used in this work has to meet the following criteria: $V_0 = 0.1$ L; $f_{\text{max}} = 200$ strokes per minute, $D_{\text{exp}}/D_{\text{phys}} \leq 0.52$ and $\nu_{\text{exp}}/\nu_{\text{phys}} \leq 0.64$. As stated previously in this work we employed a 1:2 geometrical scale model. In addition, typical values of the kinematic viscosity of blood at 37 °C and water at 25 °C were taken as being $3.9 \cdot 10^{-6}$ m^2 s^{-1} and $8.9 \cdot 10^{-7}$ m^2 s^{-1}, respectively, thus the viscosity ratio is $\nu_{\text{water}}/\nu_{\text{blood}} = 0.23$. The peak Reynolds number in our flows was of order $\mathcal{O}\{10^4\}$ and the Womersley number of order $\mathcal{O}\{10\}$, which closely matches those found in the real physiological system.

2.1.3. Flow measurement

Considerable effort was made to minimise any optical distortions that would arise during the laser-based measurements from the round AD model. This was achieved by matching the refractive index of the AD model material (PFA), $n_{\text{PFA}} = 1.34$ to the liquid used (DI water), $n_{\text{water}} = 1.33$. The AD model was placed in DI water, filling the borosilicate glass box with square sides, see Fig. 1. The slight mismatch in the refractive indices was corrected by an image anti-distortion correction post-processing algorithm. Such refractive-index matching approach is commonly used in laser-based flow dynamics imaging measurements in various flow applications (Charogiannis et al., 2015; Voulgaropoulos et al., 2019).

The flow in the AD model was measured using a PIV system (by LaVision) that employs a double-pulsed frequency-doubled Nd:YAG laser (Nano-L-50-100PV, Litron Lasers) with an excitation wavelength at $\lambda = 532$ nm, a pulse duration of 4 ns, a maximum pulse energy of 50 mJ, and a maximum frequency of 100 Hz. A sheet-optic arrangement generated light sheets with a thickness of 0.1 mm. More details on the laser system can be found in Voulgaropoulos et al. (2019).

The liquid (DI water) was seeded with inert hollow borosilicate glass spheres (supplied by LaVision) with a mean diameter of $D_{\text{p}} = 11 \pm 2$ µm and density $\rho_{\text{p}} = 1100 \pm 50$ kg m^{-3}. The ability of the particles to accurately follow the flow can be estimated via the Stokes number, which is defined as $St = \tau_{\text{p}} U_{\text{tl}}/D_{\text{tl}}$. Here τ_{p} is the response (relaxation) time of the particles $\tau_{\text{p}} = D_{\text{p}}^2 \rho_{\text{p}}/18\mu_{\text{w}}$; D_{tl} is the effective diameter of the true lumen and U_{tl} is the characteristic velocity of the flow calculated as $U_{\text{tl}} = Q_{\text{max}}/\left(\pi D_{\text{tl}}^2/4\right)$. The Stokes number in the described experimental conditions is $St = 3 \cdot 10^{-4}$. Typically, a Stokes number much lower than unity ($St << 1$) describes particles that will faithfully respond to the fluid's velocity. Less than 1% tracing errors are expected (Voulgaropoulos et al., 2019).

In this study, the elastically scattered light was recorded by a monochromatic CMOS camera (VC-Imager Pro HS 500, LaVision) positioned at 90 ° to the laser light sheet, see Fig. 1(d). The camera, having a resolution of 1280 × 1024 pixels, was equipped with a macro lenses (EX Sigma DG Macro 105 mm f/2.8; Nikon, Japan). Two separate measurements were taken for the area in the downstream direction of the entry tear and upstream direction of the re-entry tear; see Fig. 1(e). In both cases, the PIV imaging windows were equal to 20.7 × 25.9 mm, that corresponds to a spatial resolution of 20.2 µm/pixel.

2.2. Data and uncertainty analysis

During each measurement, a set of 600 image pairs (the PIV measurements were performed in a double-frame camera mode) was taken at a frequency of 100 Hz. A number of time delays between PIV image-pairs (or between laser pulses) were employed, specifically dt = 100, 250, 750 and 1000 µs, resulting in different datasets. The higher velocities present during the peak systole were resolved by using data generated with lower dt values (100 and 250 µs); while the lower velocities encountered during the relaminarisation in the false lumen were resolved in high detail by using data generated with higher dt values (750 and 1000 µs). Specifically, the dt values were chosen so that the maximum particle displacement in a selected interrogation window remains less than a quarter of the length of the interrogation window (Prasad, 2000) and thus any PIV correlation errors were minimised (Adrian et al., 2011). Approximately seven cardiac cycles were recorded for each experimental condition, and measurements were made twice using the four aforementioned dt values.

The raw images (e.g., Fig. 2(a)), were processed using DaVis 7.2 (LaVision). Initially, masks were constructed in order to limit the PIV calculation only to the regions containing particles, excluding the PMMA flap together with the tear openings and regions outside the inner PFA walls. The masked raw images were then pre-processed in order to increase the signal-to-noise ratio using an in-built algorithm that subtracted a sliding local pixel count minimum over three images (e.g., see Fig. 2(b)). This is a standard approach in PIV algorithms, as such filtering increases the intensity of the signal (particles) to noise (background) ratio, and therefore reduces the errors in the PIV measurements, i.e., improved ratios of primary to secondary peaks in the cross-correlation stages. This approach has been used in several other works (Charogiannis et al., 2015; Voulgaropoulos et al., 2019).

The velocity vector maps were obtained from the pre-processed image pairs using a cross-correlation function utilising a multi-pass technique based on the employment of the information regarding the PIV displacement from the preceding cross-correlation passes. During the initial pass, the PIV interrogation window was set to 64 × 64 pixels. The PIV interrogation window was then reduced to

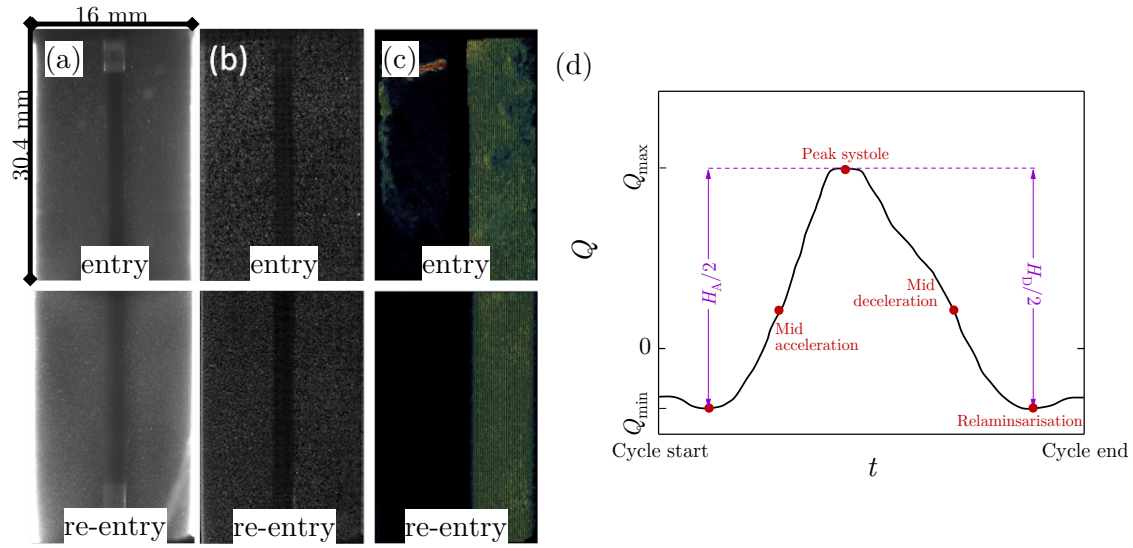

Figure 2: Image analysis procedure followed: (a) raw PIV image; (b) pre-processed PIV image (contrast and brightness adjusted for clarity purposes); and (c) velocity vector map, shown for both the entry (top) and re-entry tear (bottom). (d) Characteristic cardiac time-instances (shown on an experimental flow-rate time-trace) selected for comparison between the experimental measurements and computational predictions. Mid-acceleration and mid-deceleration are defined at the mid-height interval between relaminarisation and peak systole.

16×16 pixels with 50% overlap of the adjacent areas during the consecutive four passes, yielding a final spatial resolution of 161.6 µm between vectors.

The following processing steps were applied during the initial three PIV passes to obtain the temporal velocity maps: (i) A median filter was applied where a vector was removed if its magnitude exceeded two times the root-mean-square (RMS) of its neighbours. A vector was then re-inserted based on a consecutive cross-correlation peak if its magnitude was smaller than three times the RMS of its neighbours. (ii) Groups of less than 5 vectors were removed. (iii) An interpolation/extrapolation routine filled empty regions. (iv) A 3×3 smoothing filter was applied. A similar vector post-processing routine was applied to the final PIV pass with the exception of the extrapolation, vector group removal and smoothing steps. Nevertheless, the median parameters were set to 1.2 and 1.75 for the removal and reinsertion criteria, respectively. A typical outcome from the data processing algorithm (velocity vector map) can be seen in Fig. 2(c).

Uncertainty in the calculated PIV velocity fields arises from a multitude of factors, such as the ability of particles to follow the fluid motion, the laser sheet position, thickness and alignment, the time delay between two successive PIV imaging frames ($\mathrm{d}t$), the size of the interrogation window and the accuracy of the sub-pixel interpolation of the cross-correlation peak, amongst other. As mentioned previously, the experiment was designed to minimise these errors. The uncertainty of the individual instantaneous vectors was estimated by DaVis 8.3 (LaVision) using the correlated statistics method (Wieneke, 2014; Sciacchitano et al., 2015). The mean uncertainty was estimated at 11.5% with a median value at 9.0% for instantaneous velocities larger than 0.5 $\mathrm{m\,s^{-1}}$ for measurements with $\mathrm{d}t = 100$ µs, i.e., conditions used to resolve peak systole. For smaller velocities (during the diastole), the relative uncertainty is estimated to increase to about 30%, despite the use of bespoke correlation ($\mathrm{d}t$).

The velocity profiles for the individual entry and re-entry tear windows were obtained from spatial averaging of the last four downstream and upstream vectors within the corresponding velocity vector maps, respectively [Fig. 1(e)]. The global instantaneous velocity profiles for a given AD geometry were constructed by averaging velocity profiles over individual time-instances in a cardiac cycle of both tears [Fig. 1(e)]. The true and false lumen velocity profiles recovered from the entry and re-entry PIV imaging windows are within 0.043 and 0.014 $\mathrm{m\,s^{-1}}$ (mean absolute deviation) from the average velocity profiles, which are reported in this paper. The volumetric flow-rates, Q, are based on half of the channel cross-section (Fig. 2(b)), and were calculated based on the instantaneous velocity profiles $u\,(r)$ from:

$$Q = \pi \int_{r=d_1/2}^{r=R} r u\,(r)\,\mathrm{d}r, \tag{11}$$

where r is the variable radial distance from the centreline and R is the inner radius of the aortic channel such that the fluid flow domain extends over the range $0 < r < R$. The phase-locked averaging was performed via MATLAB *a-posteriori*. A cycle-to-cycle variability of less than 10% was calculated throughout the cycle, while the standard error of the phase-locked means reported was $\sim 4\%$.

An example of a flow-rate time-trace of a given AD model is shown in Fig. 2(d), which also shows the four characteristic cardiac time-instances (mid-acceleration, peak systole, mid-deceleration and relaminarisation) that

are used for a qualitative as well as quantitative comparison between PIV measurements and CFD modelling.

2.3. Computational methods

2.3.1. Geometry

The computational domain was created using ANSYS ICEM CFD to the specifications of the one used in the experiments (described in Section 2.1). The descending aorta was divided into two parts – the true and the false lumen. Two circular tears were created on the septum or dissection insert, one at the top and another at the bottom, to allow communication between the two lumina. Four different geometries were generated of d_2:d_1 tear-size ratios, identical to those used in the experiments, to allow direct comparisons between experiments and simulations.

The mesh was generated using ANSYS ICEM CFD and comprises three-dimensional (3-D) tetrahedral cells with ten prismatic layers extruded from the boundary wall. A local refinement in the tear regions was applied to ensure a finer resolution in regions with large velocity gradients. As a transitional turbulence model was implemented, the height of the prismatic cell layer adjacent to the wall, which can be represented by the dimensionless wall distance y^+, was kept below 2 in all geometries. Furthermore, a mesh sensitivity test is carried out for all geometries and the final mesh was selected when the relative differences of the maximum velocities and time-averaged wall shear stress were smaller than 5%. The number of elements for the final mesh varied from 2 to 2.5 million depending on the size of the tears.

2.3.2. Numerical framework

The unsteady incompressible Reynolds-averaged Navier-Stokes equations were solved using a finite volume-based CFD code ANSYS Fluent 13.0. They are given by Eqs. 12 and 13 in tensor notation and Cartesian coordinates (Ferziger et al., 2002):

$$\frac{\partial\left(\overline{u}_i\right)}{\partial x_i} = 0, \tag{12}$$

$$\frac{\partial \rho\overline{u}_i}{\partial t} + \frac{\partial}{\partial x_j}\left(\rho\overline{u}_i\overline{u}_j + \rho\overline{u_i'u_j'}\right) = -\frac{\partial\overline{p}}{\partial x_j} + \frac{\partial\overline{\tau}_{ij}}{\partial x_j}, \tag{13}$$

where p is the pressure and $\overline{\tau}_{ij}$ are the mean viscous stress tensor components:

$$\overline{\tau}_{ij} = \mu\left(\frac{\partial\overline{u}_i}{\partial x_j} + \frac{\partial\overline{u}_j}{\partial x_i}\right). \tag{14}$$

The stress tensor is determined by further closure equations given by the hybrid k-ω transitional SST (Shear Stress Transport) turbulence model, which uses the k-ω model for the inner boundary layer and the k-ε model for the other regions (Wilcox et al., 1998; Menter et al., 2003).

Pulsatile CFD simulations were performed and the following boundary conditions were applied:

- Rigid walls with a non-slip condition were considered.
- A parabolic velocity profile was specified at the inlet with the same flow-rate waveform used in the experimental test.
- The waveform period was 0.857 s and the output 0.84 L min^{-1}.
- The peak Reynolds number was 13,856 based on the inlet diameter of 16 mm.
- A turbulence level of 1.5% was specified at the inlet in order to trigger the transitional SST model (Nerem et al., 1972; Cheng et al., 2010).
- Opening boundary condition was applied at the outlet with a relative static pressure of 0 Pa.

The flow medium used in the CFD was water in order to match the experiments. Transient CFD simulations were performed with a time-step of 1 ms. All simulations were performed for three cardiac cycles to allow transients to decay and periodic solutions to be obtained; the results presented here are from the third cycle.

3. Results

The PIV data together with CFD results are used in this section to provide insight into key flow features through the AD and to elucidate the role of the tear sizes on these. Phenomenological observations based on velocity vector maps (both PIV and CFD) at four distinctive positions of a cardiac cycle are presented first, in Section 3.1. Following this, Section 3.2 contains a comparison of flow rates, in both the true and the false lumen, measured in the experiments and calculated in the simulations. Section 3.3 presents an analysis of the velocity profiles for both measurements and simulations. Finally, Section 3.4 contains a detailed statistical characterisation of the flow in the AD based on the CFD simulations and the calculated time-averaged wall shear stresses (TAWSS).

3.1. Phenomenological flow observations

Velocity field images at four distinctive time-instances of a cardiac cycle, mid-acceleration, peak systole, mid-deceleration and relaminarisation are shown in Fig. 3(a). These images are constructed by phase-locked time-averaging of the PIV measurements at given time-steps of the cardiac cycle. The flow fields shown correspond to the AD geometry with equal entry and re-entry tear sizes, namely the 32-32 AD geometry case. The contour colour represents the magnitude of the velocity, while the flow direction is indicated by unicolour vectors. The mean direction of the flow is from top to bottom.

An inflow jet in the false lumen can be observed in the area of the entry tear during both mid-acceleration and peak systole. The jet in the false lumen decreases in intensity during the transition from mid-acceleration towards

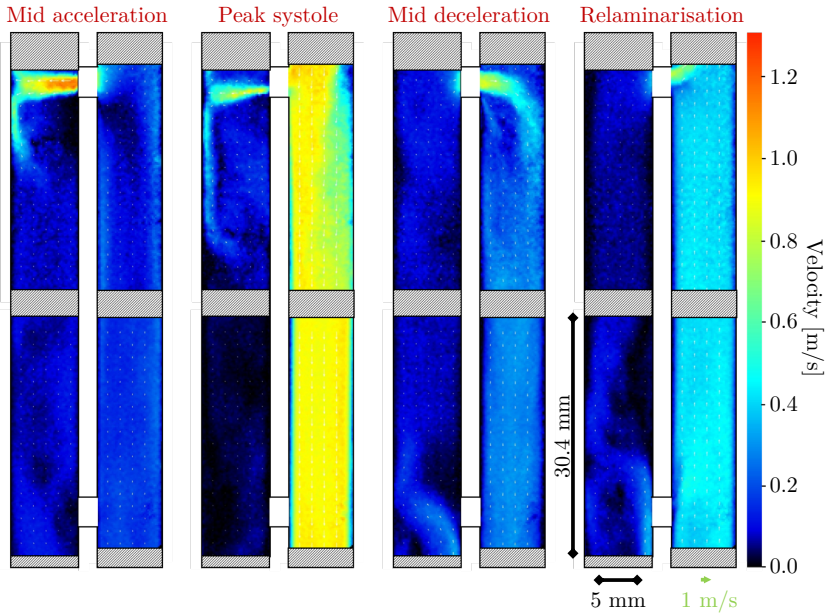

(a) PIV

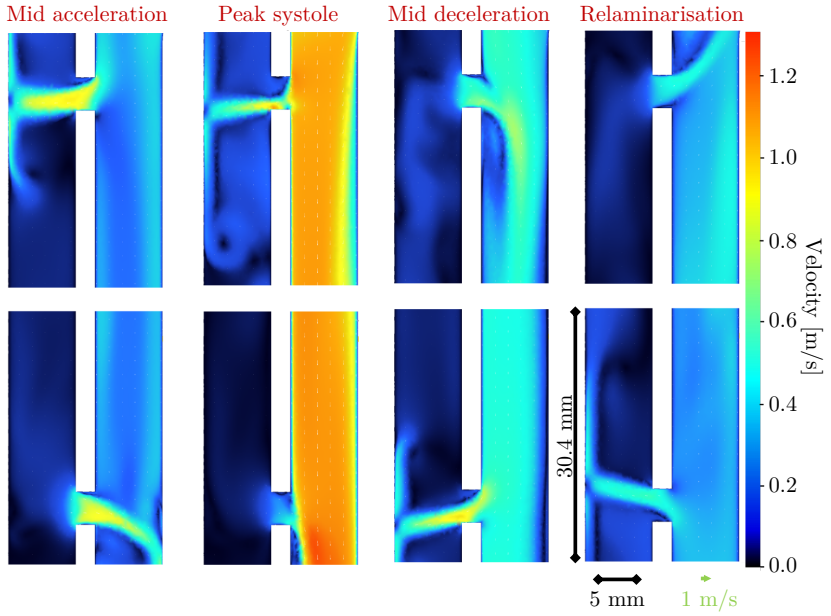

(b) CFD

Figure 3: Experimental phase-locked averaged velocity fields obtained by PIV and CFD at mid-acceleration, peak systole, mid-deceleration and relaminarisation for the 32-32 AD case. Both entry and re-entry tears have a diameter of 3.2 mm.

peak systole, occupying a full cross-section of the entry tear, however, it is located only at the lower part of the entry tear at the latter cardiac time-instant. In addition, the plume of the jet extends in length between the two aforementioned time-instances, which is accompanied by a shift of the centre of the recirculation zone by approximately 7.5 mm downstream and by an extension of the recirculation zone towards the streamwise direction. The flow reverses its direction for the mid-deceleration and relaminarisation zones, pointing from the false lumen to the true lumen. The main flow during the first time-instant is directed towards the streamwise direction, while it shifts towards the aortic arch during the second time-instant.

No strong inflow or outflow is present in the experimental results in the area of the re-entry tear for all the shown cardiac time-instances for this typical geometry (note that these observations stop holding for the other investigated tear diameters). The highest velocity in the stream wise direction in the true lumen is exhibited during the peak systole, contrary to the relaminarisation time when the direction of the flow is reversed towards the aortic arch.

The results obtained from the CFD simulations are

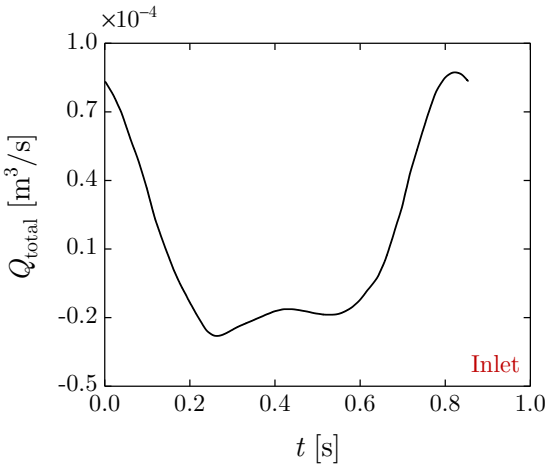

Figure 4: Total volumetric flow-rate profile in the AD model measured by PIV over one cardiac cycle. This profile is imposed at the AD model inlet in all CFD simulations.

shown in Fig. 3(b) at the same cardiac time-instants as those shown for the experimental results in Fig. 3(a). The flow enters the false lumen through the entry tear and leaves through the re-entry tear as the inlet flow-rate accelerates and reaches its peak. During this time, a recirculation zone forms at the entry tear area and grows as the peak systole arrives. The flow reverses with time and enters the false lumen through the re-entry tear and leaves through the entry tear, while the inlet flow-rate decelerates and reaches its minimum during relaminarisation. During this time, a recirculation zone is observed in the re-entry tear area, which grows as the flow rate decelerates.

When the flow enters the false lumen, the tear size determines the resistance to the flow. A larger tear means low resistance causing lower velocities. A small tear means high resistance resulting in higher velocities. For example, comparing the 32-32 and 32-64 AD geometry cases, a decrease in the velocity flow through the entry tear can be observed as the tear size increases. It is interesting to see that also the tear size determines the angle at which the jet impacts the wall. For example, during mid-deceleration and relaminarisation in Case 16-64, the jet impacts the wall with a straight angle as the flow enters the false lumen through the bottom tear. On the other hand, in the 32-32 AD case, the jet enters the false lumen with a reflex angle and moves up as the relaminarisation approaches.

3.2. Flow rates

The inlet volumetric flow-rate in the AD model is shown in Fig. 4. This flow-rate time trace is constructed by averaging PIV measurements of all investigated tear diameters for both the entry and re-entry tears of the PIV imaging windows, e.g., 112 cardiac cycle profiles are used for the one in Fig. 4 (considering only experimental results with $\mathrm{d}t$ = 100 and 250 µs). Note that the individual flow-rates are calculated using Eq. 11 and the velocity profiles obtained from spatial averaging of the last four downstream and upstream vectors within the corresponding velocity vector map of the entry and re-entry tear, respectively. The average volumetric flow-rate profile shows typical trends with mid-acceleration, peak systole, mid-deceleration and relaminarisation. The complete cardiac cycle takes 0.875 s. This flow-rate profile shown in Fig. 4 is imposed as the inlet flow-rate in the CFD simulations.

Figure 5 shows a comparison of the flow rate in the true lumen (Q_{true}) for all four investigated AD geometries, as measured from PIV and predicted by CFD. Both PIV and CFD data are extracted from results at the location defined in Fig. 1(e). There is no clear influence of the tear size on the true lumen flow-rates. The flow rates from the CFD simulations appear both qualitatively and quantitatively similar to the PIV results.

A comparison of flow-rate time traces in the false lumen (Q_{false}) is shown in Fig. 6. The lowest flow-rate in the false lumen is observed for the geometrical case which features the smallest re-entry tear, 16-64 (d_2 = 1.6 mm). A close examination and comparison between the experimental and computational results reveals some minor quantitative differences, however, these appear when the measured velocities are low and are of the order of the experimental error; the qualitative trends for the two results are in good agreement. The quantitative differences may be attributed to uncertainties in measuring low flow-rates in the false lumen as described in Section 2.2.

3.3. Velocity profiles

Velocity profiles obtained from PIV experiments and CFD simulations are compared in Fig. 7. The cardiac time-instances defined in Fig. 2(d), i.e., mid-acceleration, peak systole, mid-deceleration and relaminarisation, are used for the comparison. From Fig. 7, it can be seen that the velocity profiles exhibit different behaviours at the selected times. In particular, during peak systole it appears that the CFD predicted velocity profiles in the true lumen are more developed, illustrating higher velocities than the PIV measurements. This discrepancy could arise from relatively low number of time instances used during the phase-locked averaging (note that seven cardiac cycles are recorded during the PIV measurements), which could result in some temporal dependency of the aforementioned velocity profiles.

3.4. False lumen flow-rate

Figure 8 shows the ratio of the false lumen flow-rate (Q_{false}) to the total flow-rate (Q_{total}) calculated from the CFD simulations in all geometries at four selected cardiac time-instances. It can be observed that as the entry and re-entry tears become larger, the false lumen flow-rate increases. However, it is interesting to note that the effect of the re-entry tear size appears to be more dominant than the entry tear size in determining the fraction of flow into the false lumen. For example, the flow rate increases approximately four-fold as the re-entry tear doubles its size,

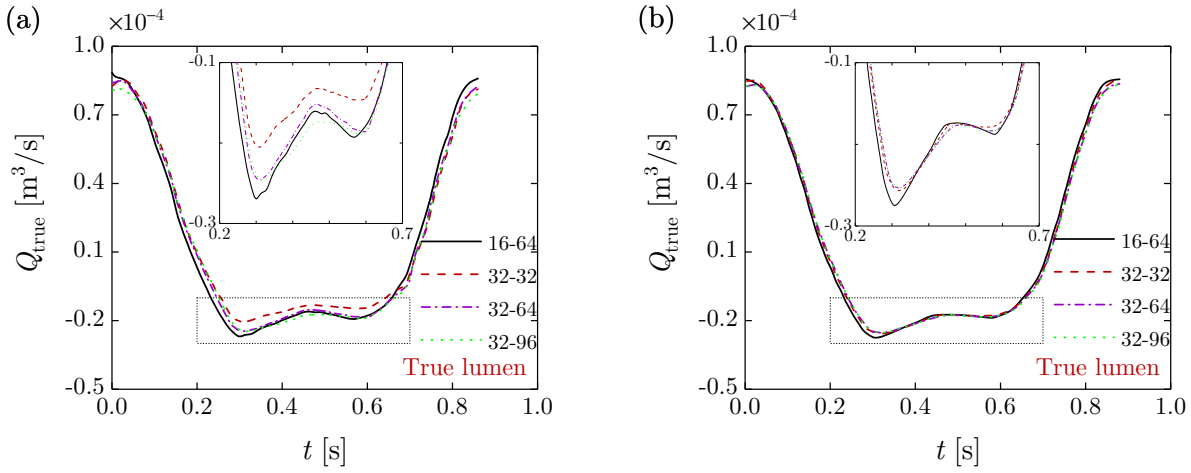

Figure 5: Comparison of volumetric flow-rates in the true lumen for the four AD geometry cases: (a) measured results from the PIV experiments; and (b) predicted results from the CFD simulations.

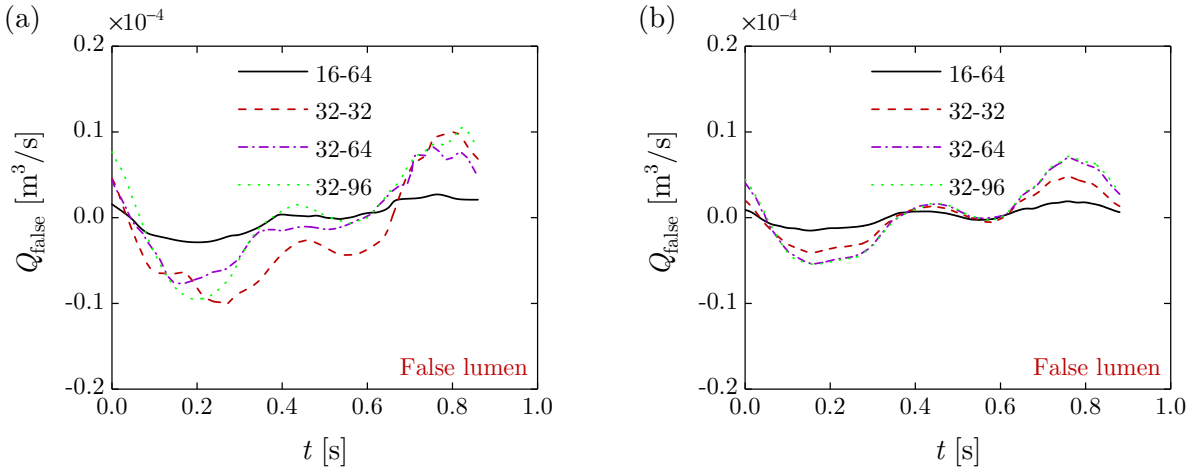

Figure 6: Comparison of the volumetric flow-rates in the false lumen for the four AD geometry cases: (a) measured results from the PIV experiments; and (b) predicted results from the CFD simulations.

i.e., when going from the 16-64 to the 32-64 AD geometry case; however, the flow rate increases only by $\sim 50\%$ as the entry tear doubles its size, i.e., between Cases 32-32 and 32-64. There is no significant increase in the flow rate as the entry tear increases further, as demonstrated by considering the 32-64 and 32-96 AD cases.

3.5. Wall shear stresses

WSS has been referenced as a crucial cause for the progression of AD. Researchers, as discussed in recent reviews (Sun and Xu, 2014; Morris et al., 2016; Sun and Chaichana, 2016), have argued that high WSS causes enlargement of the tear and false lumen, and increase in the tortuosity of the descending aorta. Also, low WSS are linked to areas of flow stagnation, which can lead to formation of thrombus.

The most significant TAWSS are located around the tears and in the false lumen wall. The WSS calculated in the ascending aorta and in the true lumen wall do not show significant changes and the values are considered normal for the aorta. Figure 9 shows the TAWSS calculated on the entry and re-entry tears, respectively. The highest TAWSS are found on the septum and specifically on the edges of the tear. It can be observed that the distribution of the TAWSS depends on the combined sizes of the tears. For example, in Case 32-32, the WSS is distributed uniformly between the entry and re-entry tears, however, in Case 16-64, high WSS values are observed around the smaller re-entry tear. Similar findings and observations are obtained when considering the 32-64 and 32-96 cases.

However, the most significant change of WSS happens in the bottom tear. In one hand, when the bottom tear increases, WSS decreases significantly. Comparing the effect of the re-entry tear sizes in Cases 16-64 and 32-64, WSS around the re-entry tear decreases by 5 Pa. In the other hand, when the entry tear increases, WSS also increases. Comparing Cases 32-32 and 32-64, the WSS around the bottom tear can be seen to increases by 3 Pa. However,

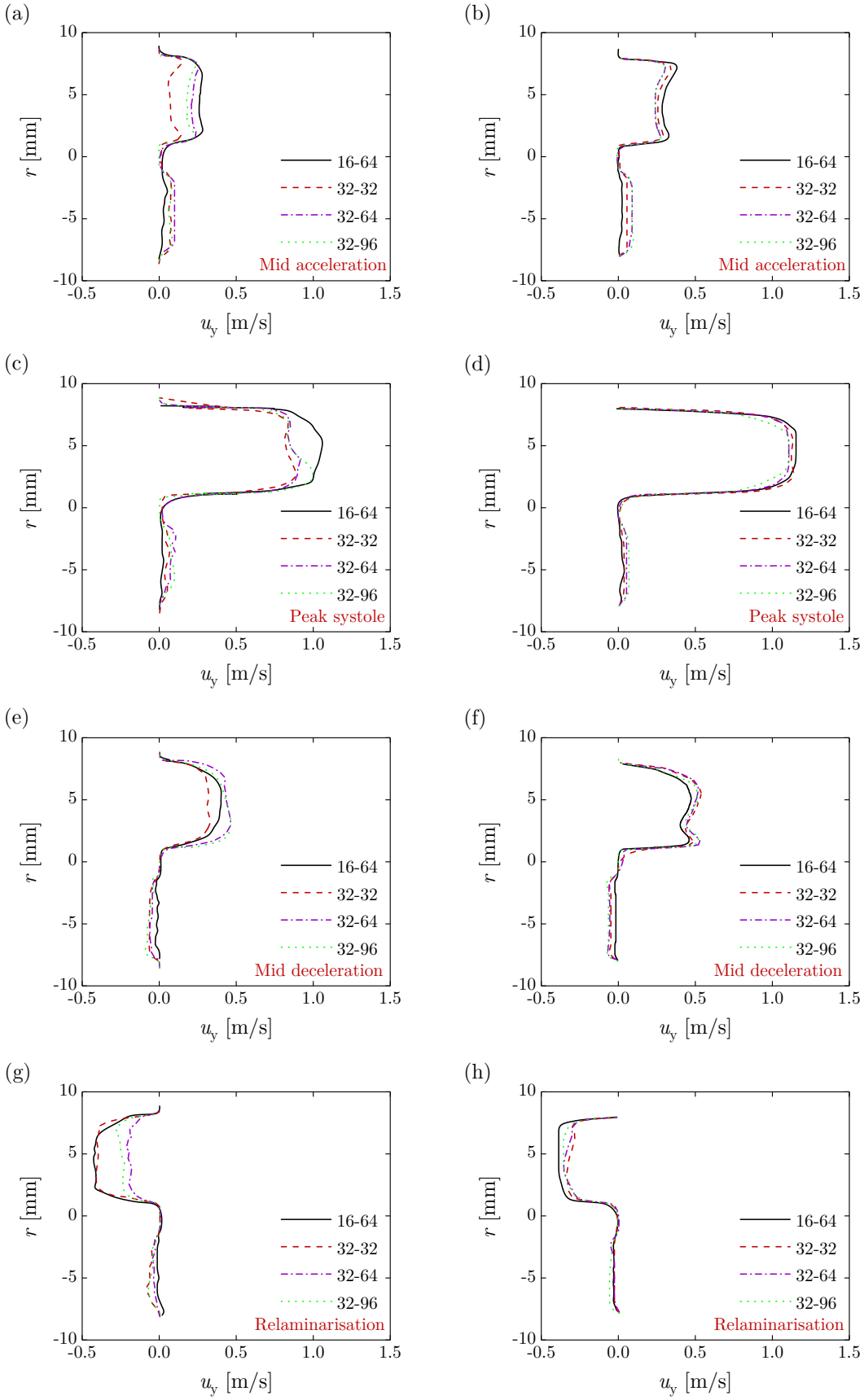

Figure 7: Comparison of velocity profiles at the selected cardiac time-instances of: (a-b) mid-acceleration; (c-d) peak systole; (e-f) mid-deceleration; and (g-h) relaminarisation. Results from the PIV experiments are on the left-hand side and from the CFD simulations are on the right-hand side.

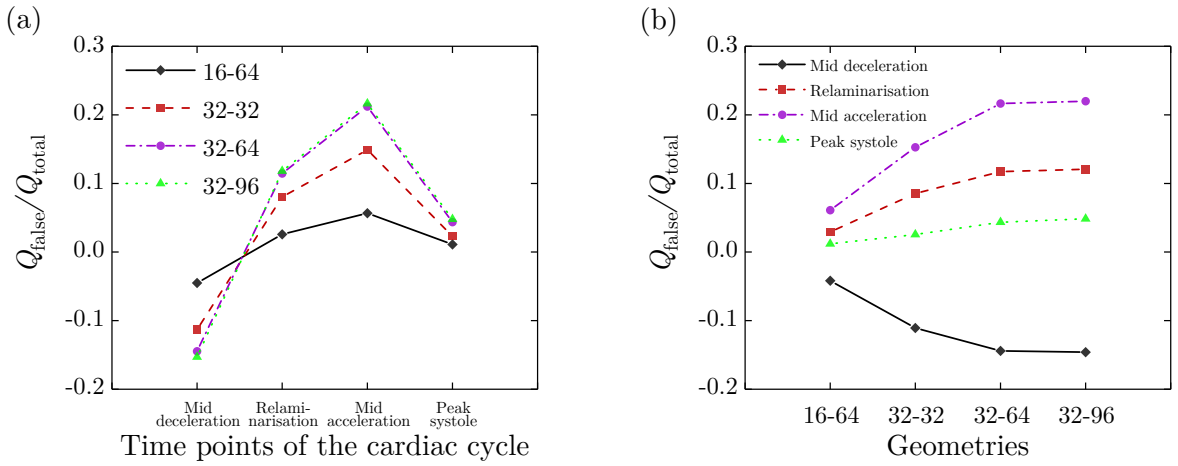

Figure 8: Ratio of the false lumen flow-rate to the total flow-rate obtained from the CFD simulations, showing a comparison of the: (a) four geometries tested; and (b) four selected cardiac time-instances.

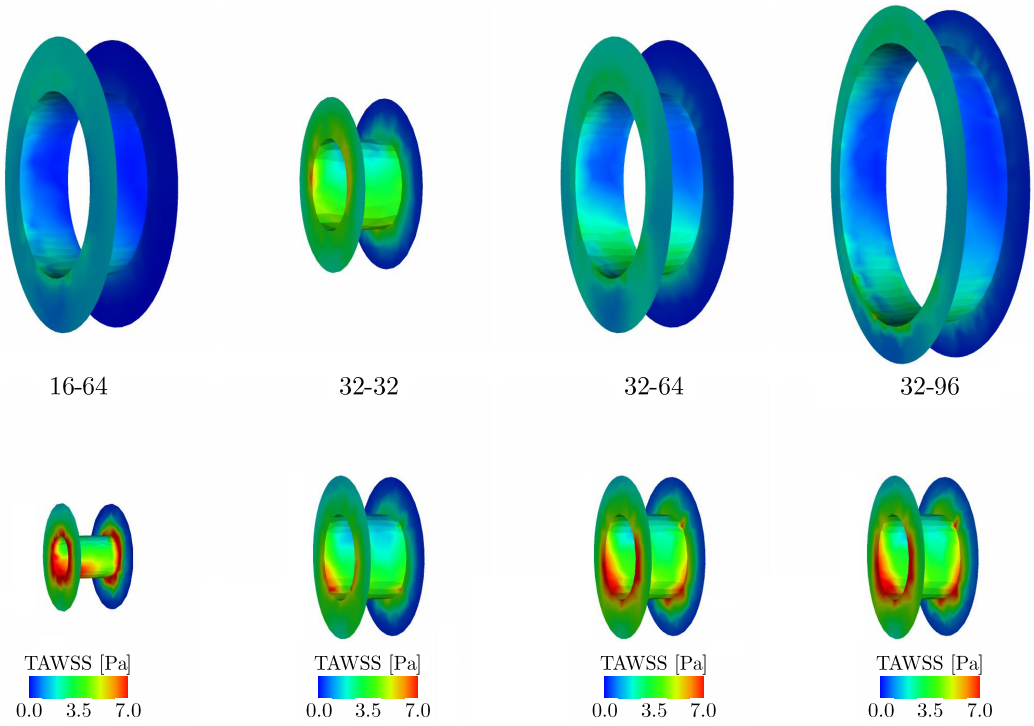

Figure 9: TAWSS obtained from the CFD simulations for each tear case. Entry and re-entry tears can be seen in the top and bottom row, respectively.

a larger entry tear (e.g., when comparing Cases 32-64 and 32-96) produces a slight increase in the WSS.

Figure 10 shows the TAWSS calculated on the false lumen wall. High TAWSS values are found opposite the entry tear and also opposite the re-entry tear. In Case 32-32, similar values of WSS are calculated at the top and bottom areas. However, as the entry tear size increases, the stress in the bottom area increases while decreases in the top area. Contrary, as the re-entry tear size increases, the stress in the bottom area decreases while increases in the top area. In Case 16-64, the shape of the stress in the bottom area is almost circular. Interestingly, in this case a jet flow impacting the the false lumen wall is observed during mid-deceleration and relaminarisation.

Table 1 summarises the maximum predicted TAWSS in different AD geometries and the re-entry to entry ratio of the tear for each case simulated. It can be observed that as the tear ratio increases the maximum values of TAWSS decrease, or in other words that the maximum TAWSS is observed for the more asymmetric entry/re-entry tear sizes. For example, Case 16-64 with the lowest ratio, 1:4, exhibits the highest TAWSS; while Case 32-32 with the

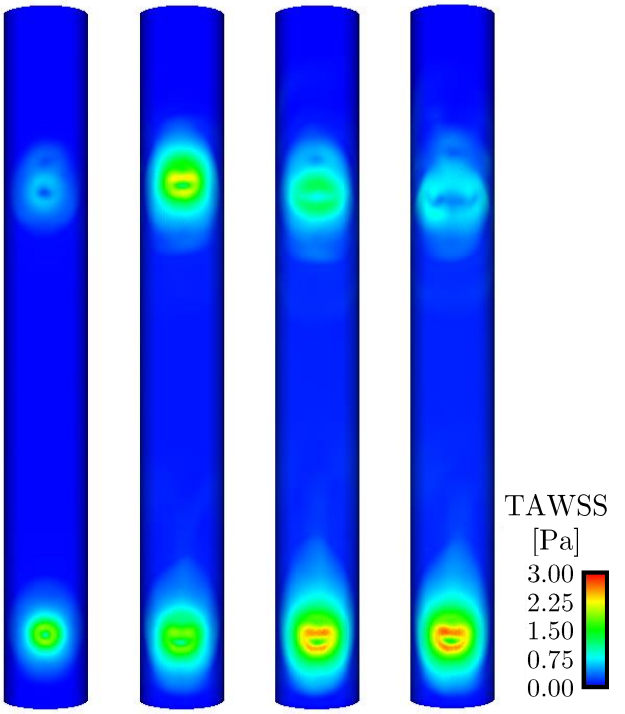

Figure 10: TAWSS (time-averaged over the cardiac cycle) obtained from the CFD simulations over the false lumen wall.

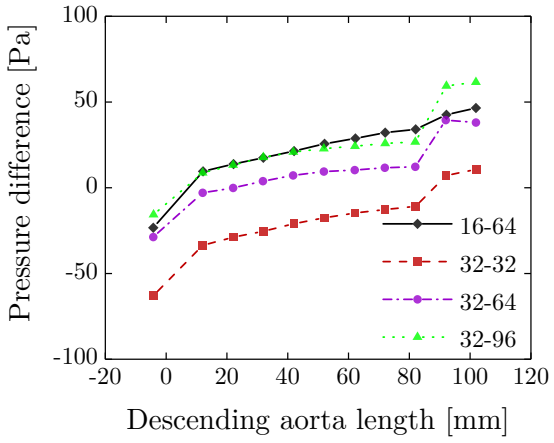

Figure 11: Time-averaged pressure difference along the length of the descending aorta.

1:1 ratio AD geometry exhibits the lowest TAWSS values.

Figure 11 shows the time-averaged pressure difference between the false lumen and the true lumen. Eleven planes are created along the dissected aorta and the pressure calculated at each plane. The entry tear is situated between Planes 1 and 2 and the re-entry tear is situated between Planes 9 and 10. After that, the pressure difference is calculated as the pressure in the false lumen minus the pressure in the true lumen. Finally, the time-averaged pressure difference is calculated. For all AD geometry cases, apart from Case 32-32, the false lumen pressure is higher than the true lumen. Interestingly, when the ratio d_2:d_1 is unity, the behaviour reverses and the true lumen pressure becomes higher than the one in the false lumen. In addition, the biggest changes in pressure occurred when passing the entry and re-entry tear. Interestingly, the increase in pressure difference can be linked to the tear size ratio d_2:d_1. As the ratio decreases, the pressure difference increases. However, there is no significant change for ratio 1:3 and 1:4 (32-96 and 16-64 cases).

Data by Tsai et al. (2008) and Rudenick et al. (2013) also support the aforementioned findings. Tsai et al. (2008) reported false lumen pressure indices (FPI, i.e., false lumen diastolic pressure over true lumen diastolic pressure) above 1 (or 100%) in the two cases investigated of 32-32 and 64-64. For the 32-32 case, they reported a pressure difference in the time-averaged values of about −74 Pa (measured upstream of the test section), which deviates less than 15% from the −63 Pa pressure difference reported in Fig. 11 for the same geometry and measurement location, which can be attributed to the difference in the properties of the working fluid used. Rudenick et al. (2013) report time-averaged FPIs below 1 for a 1:1 tear size ratio, while the FPI for a 40-100 case, similar ratio to the 32-96 case of Table 1 and Fig. 11, was approximately 1 (i.e., pressure difference between the false and true lumen close to 0).

4. Summary and Conclusions

This paper presented results from a combined experimental and complementary computational effort aimed at evaluating the effect of the entry and re-entry tear sizes and ratios in aortic dissections on critical condition parameters, such as differential flow, pressure and wall shear stress, in a model of Type B aortic dissection. To minimise the degrees of freedom that exist in complex, real (patient-specific) physiological geometries, an idealised, simplified geometric model of Type B aortic dissections was considered, in a series of flow tests in which dynamic similarity was ensured with real physiological flows, while using an appropriate pulsatile ('blood') pump specifically manufactured for such studies. The flow characteristics through the true and false lumina were investigated parametrically over a range of tears, experimentally using particle image velocimetry (PIV) and numerically using computational fluid dynamic (CFD) simulations. Equivalence between the experiment and corresponding simulations was achieved by using the same flow domains and conditions (e.g., geometry, fluid) and the experimentally derived flow-rate profile as an inlet condition in the simulations.

Pulsatile CFD simulations were performed by solving the unsteady incompressible Reynolds-averaged Navier-Stokes equations using the hybrid k-ω transitional shear stress transport (SST) turbulence model. In the experiments, PIV was employed to obtain spatiotemporally resolved information on the fluid velocity field throughout a

series of aortic dissection models, which were used in turn to validate the numerical simulation by comparing volumetric flow-rates and phase-locked averaged velocity profiles for four tear size ratios and at the four characteristic time-instances during the cardiac cycle. The comparison between PIV and CFD demonstrated good qualitative and quantitative agreement for the temporal flow-rate profiles, with some observed differences in the velocity profiles when the measured velocities were low, which were of the order of the experimental error.

The CFD results were then exploited in order to extend the experimentally available information and to perform a parametric study on the effect of the tear sizes and ratios on critical haemodynamic parameters that were found to lead to further progression of the dissection that had previously formed. It was found that as the tear size ratio decreased, the false lumen flow-rate increased, while a clear and dominant effect of the re-entry tear size was found, resulting in a stronger influence on the false lumen flow rate than that of the entry tear size. Specifically, the flow rate was found to increase by approximately four times when the re-entry tear doubled (going from the 16-64 to the 32-64 geometry case), while it only increased by about $\sim 50\%$ when the entry tear doubled in size (going from the 32-32 to the 32-64 case), with even less change in the flow rate when the entry tear was increased further.

The highest wall shear stress (WSS) was identified on the edges of the tears, which appears to be a region of great importance. Interestingly, and similar to the flow rate results, the WSS results strongly suggested that the effect of the re-entry tear size has a primary role in controlling the WSS compared to the size of the entry tear. In addition, a relation between the ratio of the re-entry tear size to the entry tear size, and the WSS/pressure difference in the model was found. Ratios closer to unity resulted in lower time-averaged WSS and pressure difference, while the opposite behaviour was observed for asymmetric entry/re-entry tear-size ratios. Still, it was found that there was a critical point (observed between tear size ratios of 1:3 and 1:4), where a further decrease of the tear size ratio did not further increase the pressure difference.

Owing to technical challenges in the fabrication process, several geometric simplifications were made; these included exclusion of the vessel branches and planar geometry, which will have an impact on the resulting fluid dynamics. The working fluid (water) has a different rheological behaviour from that of blood. Although flow similarity was ensured by matching the Reynolds and Womersley numbers to those of aortic blood flow, the predicted wall shear stress and pressure values will deviate from those under physiological conditions, especially in low shear regions where the shear-thinning effect of blood is non-negligible. Furthermore, a rigid model was used, neglecting the effect of aortic wall compliance and dissection septum movement on flow. Nevertheless, the simplified model employed in this study retained the most important features of type B aortic dissection and allowed us to change the size of entry and re-entry tears in a controlled manner.

There is great value in and a need for further research into aortic dissections as a serious medical condition, which can quickly lead to death from constricting blood flow to the heart or from complete rupture of the aorta (White et al., 2013). Specifically, the inherently complex and coupled nature of the many geometric, physiological and haemodynamic factors that can contribute to the disease's progression warrants an urgent and much improved understanding of key flow characteristics over a range of Type B AD geometries and how these can lead to progressive aortic dilatation and further complications. Future work will aim at employing a more realistic dissection model to elucidate the role of other tear-related parameters, such as the number of re-entry tears and the location of tears.

Acknowledgement

This work was supported by the Research Councils UK (RCUK) [grant number EP/E500641/1]. Data supporting this publication can be obtained on request from ceplab@imperial.ac.uk.

References

Adrian, L., Adrian, R. J., Westerweel, J., 2011. Particle image velocimetry. No. 30. Cambridge university press.

Alimohammadi, M., Agu, O., Balabani, S., Díaz-Zuccarini, V., 2014. Development of a patient-specific simulation tool to analyse aortic dissections: assessment of mixed patient-specific flow and pressure boundary conditions. Medical engineering & physics 36 (3), 275–284.

Alimohammadi, M., Sherwood, J. M., Karimpour, M., Agu, O., Balabani, S., Díaz-Zuccarini, V., 2015. Aortic dissection simulation models for clinical support: fluid-structure interaction vs. rigid wall models. Biomedical engineering online 14 (1), 34.

Blount, K. J., Hagspiel, K. D., 2009. Aortic diameter, true lumen, and false lumen growth rates in chronic type b aortic dissection. American Journal of Roentgenology 192 (5), W222–W229.

Bonfanti, M., Balabani, S., Greenwood, J. P., Puppala, S., Homer-Vanniasinkam, S., Díaz-Zuccarini, V., 2017. Computational tools for clinical support: a multi-scale compliant model for haemodynamic simulations in an aortic dissection based on multi-modal imaging data. Journal of The Royal Society Interface 14 (136), 20170632.

Bonfanti, M., Franzetti, G., Maritati, G., Homer-Vanniasinkam, S., Balabani, S., Díaz-Zuccarini, V., 2019. Patient-specific haemodynamic simulations of complex aortic dissections informed by commonly available clinical datasets. Medical engineering & physics 71, 45–55.

Chang, C.-P., Liu, J.-C., Liou, Y.-M., Chang, S.-S., Chen, J.-Y., 2008. The role of false lumen size in prediction of in-hospital complications after acute type b aortic dissection. Journal of the American College of Cardiology 52 (14), 1170–1176.

Charogiannis, A., An, J. S., Markides, C. N., 2015. A simultaneous planar laser-induced fluorescence, particle image velocimetry and particle tracking velocimetry technique for the investigation of thin liquid-film flows. Experimental Thermal and Fluid Science 68, 516–536.

Cheng, Z., Juli, C., Wood, N., Gibbs, R., Xu, X., 2014. Predicting flow in aortic dissection: comparison of computational model with pc-mri velocity measurements. Medical engineering & physics 36 (9), 1176–1184.

Cheng, Z., Riga, C., Chan, J., Hamady, M., Wood, N. B., Cheshire, N. J., Xu, Y., Gibbs, R. G., 2013. Initial findings and potential applicability of computational simulation of the aorta in acute type b dissection. Journal of vascular surgery 57 (2), 35S–43S.

Cheng, Z., Tan, F., Riga, C., Bicknell, C., Hamady, M., Gibbs, R., Wood, N., Xu, X., 2010. Analysis of flow patterns in a patient-specific aortic dissection model. Journal of biomechanical engineering 132 (5).

Cheng, Z., Wood, N. B., Gibbs, R. G., Xu, X. Y., 2015. Geometric and flow features of type b aortic dissection: initial findings and comparison of medically treated and stented cases. Annals of biomedical engineering 43 (1), 177–189.

Clough, R. E., Waltham, M., Giese, D., Taylor, P. R., Schaeffter, T., 2012. A new imaging method for assessment of aortic dissection using four-dimensional phase contrast magnetic resonance imaging. Journal of vascular surgery 55 (4), 914–923.

Fernandes, L., Bessa, G., Gomes, B., Azevedo, L., 2019. Stereoscopic piv study of the influence of aortic valve tilt angle on the flow pattern in the ascending aorta region. In: 13th International Symposium on Particle Image Velocimetry – ISPIV 2019, Munich, Germany.

Ferziger, J. H., Perić, M., Street, R. L., 2002. Computational methods for fluid dynamics. Vol. 3. Springer.

Hagan, P. G., Nienaber, C. A., Isselbacher, E. M., Bruckman, D., Karavite, D. J., Russman, P. L., Evangelista, A., Fattori, R., Suzuki, T., Oh, J. K., et al., 2000. The international registry of acute aortic dissection (irad): new insights into an old disease. Jama 283 (7), 897–903.

Karmonik, C., Partovi, S., Müller-Eschner, M., Bismuth, J., Davies, M. G., Shah, D. J., Loebe, M., Böckler, D., Lumsden, A. B., von Tengg-Kobligk, H., 2012. Longitudinal computational fluid dynamics study of aneurysmal dilatation in a chronic debakey type iii aortic dissection. Journal of vascular surgery 56 (1), 260–263.

Khan, I. A., Nair, C. K., 2002. Clinical, diagnostic, and management perspectives of aortic dissection. Chest 122 (1), 311–328.

Kousera, C., Wood, N., Seed, W., Torii, R., O'regan, D., Xu, X., 2013. A numerical study of aortic flow stability and comparison with in vivo flow measurements. Journal of biomechanical engineering 135 (1).

Menter, F. R., Kuntz, M., Langtry, R., 2003. Ten years of industrial experience with the sst turbulence model. Turbulence, heat and mass transfer 4 (1), 625–632.

Moravia, A., Pan, W., Le Berre, H. W., Marine, M., Bou-Saïd, B., El Hajem, M., Escriva, X., Kulisa, P., Simoëns, S., Lermusiaux, P., Millon, A., Naudin, I., 2019. In vitro assessment of abdominal aorta non-newtonian hemodynamics based on particle image velocimetry. In: European Symposium of Biomechanics 2019, Vienne, Austria.

Morris, P. D., Narracott, A., von Tengg-Kobligk, H., Soto, D. A. S., Hsiao, S., Lungu, A., Evans, P., Bressloff, N. W., Lawford, P. V., Hose, D. R., et al., 2016. Computational fluid dynamics modelling in cardiovascular medicine. Heart 102 (1), 18–28.

Nerem, R., Seed, W., Wood, N., 1972. An experimental study of the velocity distribution and transition to turbulence in the aorta. Journal of Fluid Mechanics 52 (1), 137–160.

Ong, C., Kabinejadian, F., Xiong, F., Wong, Y., Toma, M., Nguyen, Y., Chua, K., Cui, F., Ho, P., Leo, H., 2019. Pulsatile flow investigation in development of thoracic aortic aneurysm: An in-vitro validated fluid structure interaction analysis. Journal of Applied Fluid Mechanics 12 (6), 1855–1872.

Paras, S. V., Kanaris, A. G., 2019. Experimental and numerical studies in biomedical engineering.

Prasad, A. K., 2000. Particle image velocimetry. Current Science 79, 51–60.

Prêtre, R., Von Segesser, L. K., 1997. Aortic dissection. The Lancet 349 (9063), 1461–1464.

Ramanath, V. S., Oh, J. K., Sundt III, T. M., Eagle, K. A., 2009. Acute aortic syndromes and thoracic aortic aneurysm. In: Mayo Clinic Proceedings. Vol. 84. Elsevier, pp. 465–481.

Rudenick, P. A., Bijnens, B. H., García-Dorado, D., Evangelista, A., 2013. An in vitro phantom study on the influence of tear size and configuration on the hemodynamics of the lumina in chronic type b aortic dissections. Journal of vascular surgery 57 (2), 464–474.

Salameh, E., Khoury, W., Saade, C., Oweis, G. F., 2017. Piv and lif measurements in aortic dissection models. In: ASME 2017 International Mechanical Engineering Congress and Exposition. American Society of Mechanical Engineers Digital Collection.

Salameh, E., Saade, C., Oweis, G. F., 2019. Experimental insight into the hemodynamics and perfusion of radiological contrast in patent and non-patent aortic dissection models. Cardiovascular engineering and technology 10 (2), 314–328.

Sciacchitano, A., Neal, D. R., Smith, B. L., Warner, S. O., Vlachos, P. P., Wieneke, B., Scarano, F., 2015. Collaborative framework for piv uncertainty quantification: comparative assessment of methods. Measurement Science and Technology 26 (7), 074004.

Sueyoshi, E., Sakamoto, I., Uetani, M., 2009. Growth rate of affected aorta in patients with type b partially closed aortic dissection. The Annals of thoracic surgery 88 (4), 1251–1257.

Sun, N., Wood, N. B., Hughes, A. D., Thom, S. A., Xu, X. Y., 2006. Fluid-wall modelling of mass transfer in an axisymmetric stenosis: effects of shear-dependent transport properties. Annals of biomedical engineering 34 (7), 1119–1128.

Sun, Z., Chaichana, T., 2016. A systematic review of computational fluid dynamics in type b aortic dissection. International journal of cardiology 210, 28–31.

Sun, Z., Xu, L., 2014. Computational fluid dynamics in coronary artery disease. Computerized medical imaging and graphics 38 (8), 651–663.

Tan, F., Torii, R., Borghi, A., Mohiaddin, R., Wood, N., Xu, X., 2009. Fluid-structure interaction analysis of wall stress and flow patterns in a thoracic aortic aneurysm. International journal of applied mechanics 1 (01), 179–199.

Tolenaar, J. L., Van Keulen, J. W., Jonker, F. H., Van Herwaarden, J. A., Verhagen, H. J., Moll, F. L., Muhs, B. E., Trimarchi, S., 2013. Morphologic predictors of aortic dilatation in type b aortic dissection. Journal of vascular surgery 58 (5), 1220–1225.

Torii, R., Wood, N. B., Hadjiloizou, N., Dowsey, A. W., Wright, A. R., Hughes, A. D., Davies, J., Francis, D. P., Mayet, J., Yang, G.-Z., et al., 2009. Fluid–structure interaction analysis of a patient-specific right coronary artery with physiological velocity and pressure waveforms. Communications in numerical methods in engineering 25 (5), 565–580.

Tran, T. P., Khoynezhad, A., 2009. Current management of type b aortic dissection. Vascular health and risk management 5, 53.

Tsai, T. T., Schlicht, M. S., Khanafer, K., Bull, J. L., Valassis, D. T., Williams, D. M., Berguer, R., Eagle, K. A., 2008. Tear size and location impacts false lumen pressure in an ex vivo model of chronic type b aortic dissection. Journal of vascular surgery 47 (4), 844–851.

Tse, K. M., Chang, R., Lee, H. P., Lim, S. P., Venkatesh, S. K., Ho, P., 2012. A computational fluid dynamics study on geometrical influence of the aorta on haemodynamics. European Journal of Cardio-Thoracic Surgery 43 (4), 829–838.

Voulgaropoulos, V., Zadrazil, I., Le Brun, N., Bismarck, A., Markides, C. N., 2019. On the link between experimentally-measured turbulence quantities and polymer-induced drag reduction in pipe flows. AIChE Journal 65 (9), 16662.

White, A., Broder, J., Mando-Vandrick, J., Wendell, J., Crowe, J., 2013. Acute aortic emergencies—part 2 aortic dissections. Advanced emergency nursing journal 35 (1), 28–52.

Wieneke, B., 2014. Generic a-posteriori uncertainty quantification for piv vector fields by correlation statistics. In: 17th International Symposium on Applications of Laser Techniques to Fluid Mechanics, Lisbon, Portugal, July. Vol. 710. p. 2014.

Wilcox, D. C., et al., 1998. Turbulence modeling for CFD. Vol. 2. DCW industries La Canada, CA.

Yip, R., Mongrain, R., Ranga, A., Brunette, J., Cartier, R., 2004. Development of anatomically correct mock-ups of the aorta for piv investigations. Proceedings of the Canadian Engineering Education Association (CEEA).